AIAA JOURNAL
Vol. 48, No. 9, September 2010

Large-Eddy Simulation of Supercritical-Pressure Round Jets

Thomas Schmitt[*]
Centre Européen de Recherche et de Formation Avancée en Calcul Scientifique,
31057 Toulouse Cedex, France
Laurent Selle[†]
Institut de Mécanique des Fluides de Toulouse, 31400 Toulouse, France
and
Anthony Ruiz[‡] and Bénédicte Cuenot[§]
Centre Européen de Recherche et de Formation Avancée en Calcul Scientifique,
31057 Toulouse Cedex, France

DOI: 10.2514/1.J050288

This paper presents the numerical computation of a turbulent jet of nitrogen into nitrogen under supercritical pressure. The large-eddy simulation framework for turbulence modeling is used and real-gas effects are accounted for through a cubic equation of state and appropriate viscosity and conductivity coefficients. The purpose of this paper is to evaluate how low-pressure large-eddy simulation equations coupled with real-gas thermodynamics and transport compare with experiments. Although this approach does not take into account the impact of high density gradients and nonlinear thermodynamics on turbulence modeling, the results show reasonable agreement with available experimental data and reveal the importance of numerics for such computations. The simulations indicate a limited influence of the density ratio and the thermodynamic conditions on the jets spreading rate and pseudosimilarity behavior.

Nomenclature

a, b, c = coefficients for the Peng–Robinson equation of state
C_p = constant-pressure heat capacity
C_v = constant-volume heat capacity
C_w = wall-adapting local eddy-viscosity model constant
d = jet inlet diameter
d_α^{eff} = effective diameter
e = internal energy
e_t = total energy
e_k = kinetic energy
E_ρ^H = spreading rate of the density profile
E_u^H = spreading rate of the velocity profile
g = velocity-gradient tensor
K_ρ = slope of the normalized centerline-density profile
K_u = slope of the normalized centerline-velocity profile
L_ρ = half-width, half-maximum of the density profile
L_u = half-width, half-maximum of the velocity profile
P = pressure
P_c = critical pressure
P_r = reduced pressure
Pr^t = turbulent Prandtl number
q = heat flux
R = ideal-gas constant
Re = Reynolds number
r = specific gas constant
S = symmetric part of the velocity-gradient tensor
s = symmetric traceless part of the square of the velocity-gradient tensor
T = temperature
T_{aver} = duration of the averaging procedure
T_c = critical temperature
T_r = reduced temperature
T^{pb} = pseudo-boiling- point temperature
u = velocity
u^* = normalized velocity
u_{inj} = jet bulk injection velocity
Z = compressibility factor
α = thermal expansion coefficient
β = isothermal compressibility coefficient
Δ = characteristic mesh size
Δt = time step
ζ = enthalpy subgrid-scale contribution
θ^H = half-width, half-maximum spreading angle
θ^V = visual spreading angle
λ = thermal conductivity
μ = dynamic viscosity
μ^t = turbulent dynamic viscosity
ν^t = turbulent kinematic viscosity
ρ = density
ρ_c = time-averaged centerline density
ρ_{inj} = density at the jet inlet
ρ_∞ = far-field density
ρ^* = normalized density
ρ^+ = normalized centerline-density fluctuation
σ = viscous-stress tensor
τ = momentum subgrid-scale contribution
τ_c = characteristic convective time, $50d/u_{\mathrm{inj}}$
ϕ = vector of conservative variables
ω = acentric factor

Introduction

IT HAS been known since the famous cannon barrel experiments of Baron Charles Cagniard de la Tour (1822) that above a certain temperature T_c and pressure P_c, the discontinuity between gaseous and liquid phases disappears. The coordinates P_c and T_c define the *critical point*, that is the point above which the phase-change phenomenon no longer occurs. In such a thermodynamic state, talking about a gas or a liquid no longer makes sense. This state is

---

Received 3 November 2009; revision received 23 March 2010; accepted for publication 24 March 2010. Copyright © 2010 by the American Institute of Aeronautics and Astronautics, Inc. All rights reserved. Copies of this paper may be made for personal or internal use, on condition that the copier pay the \$10.00 per-copy fee to the Copyright Clearance Center, Inc., 222 Rosewood Drive, Danvers, MA 01923; include the code 0001-1452/10 and \$10.00 in correspondence with the CCC.

[*] Ph.D. Student, 42 Avenue G. Coriolis.

[†] Research Scientist, UMR CNRS/INPT/UPS, Allée Camille Soula; selle@imft.fr.

[‡] Ph.D. Student, 42 Avenue G. Coriolis.

[§] Project Leader, 42 Avenue G. Coriolis.

therefore referred to as a *supercritical fluid* (SC fluid). The exact definition of a SC fluid is still a subject of controversy in the literature and this issue is not addressed here. However, from the standpoint of computational fluid dynamics, when a departure from the perfect-gas law occurs, modifications must be made in the numerical solvers.

Rocket engines were the first (and for a long time also virtually the only) thermal engines working under supercritical conditions. However, the need for higher efficiency and lower emissions leads to increased pressure and temperature levels in other engines such as gas turbines, diesel piston engines and aeronautical turbines. Therefore, these industries are facing the scientific challenge of SC turbulent flows. For a proper description of SC fluid dynamics, two major modifications must be made to the standard low-pressure Navier–Stokes equations [1–4]:

1) An equation of state (EOS) that accounts for real-gas effects must be implemented.

2) Transport models for mass and heat transfers must be modified.

It is important that these models (EOS and transport) are made consistent through the appropriate thermodynamic relations.

The equation of state can be considered as the cornerstone of SC fluid modeling for it ensures the accuracy of the thermodynamics. Indeed, the density or the pressure dependence of the heat capacities are directly driven by the EOS [5]. Another example is the computation of combustion instabilities: the speed of sound computed from the EOS is a key parameter to the prediction of acoustic modes. For example, the influence of acoustic perturbations on a single-species jet was studied by Davis and Chehroudi [6] highlighting a reduced effect under SC conditions in comparison with subcritical state, suggesting that the coupling mechanism between acoustics and jets may be different for SC-pressure jets than for subcritical pressure jets. From a practical point of view, the equation of state must compromise between accuracy and computational cost and cubic equations of state are usually good candidates [3,5]. Strong modifications of the transport properties also occur at SC pressure: the dynamic viscosity and thermal conductivity may be enhanced [5], Soret and Dufour effects may become important, and modeling mass diffusivity is much more arduous than for low-pressure cases [7,8].

The impact of thermodynamics in compressible (reactive) flows is so important that in principle turbulence models should be revised. Experimental observations of SC turbulent flows suggest a wealth of new flow structures compared with low-pressure gaseous-turbulence [9,10]. For example, in SC jets comblike structures develop on the edge of the jet that are not observed at low pressure [11]. It has also been shown in numerical simulations that the high density gradient leads to a local reorganization of the turbulence [7,12]. Consequently, from both phenomenological and theoretical perspectives, turbulence models should take into account the thermodynamic state of the fluid. However, only a priori studies are available at the moment on this issue [13] and no turbulence model specific to SC fluids exists. Therefore, existing perfect-gas models are still used.

In this paper, a three-dimensional single-species simulation of axisymmetric jets at SC pressure is performed. Such a configuration is of particular interest for both validation and theoretical purposes, since the complicated nature of multispecies transport in the SC regime is not present. Experiments on single-species SC-pressure round jets have been carried out both at DLR, German Aerospace Center [14,15] and U.S. Air Force Research Laboratory [9,11]. The impact of the SC pressure on the jet topology was evidenced, showing that rather than breaking into several drops, the ligaments classically observed in two phase jet dissolve in the ambient gas, with no longer evidence of drops creation. Moreover, quantitative measurements of density [10,14,15], density spreading rate and density decay coefficients are available [9,16]. Visual spreading rates were obtained by Chehroudi et al. [17] and were shown to be reduced as the density ratio between injection and ambient gas was increased.

Because of its uncontroversial success in quantitatively predicting flow features in both reacting and non reacting conditions, the large-eddy simulation (LES) technique was chosen for this study. Zong [18] and Zong and Yang [19] used the LES approach to compute two turbulent nitrogen jets initially at subcritical temperature injected into SC nitrogen with chamber pressures of 69 and 93 bar (for nitrogen, $P_c = 33.958$ bar and $T_c = 126.192$ K). Good agreements with the correlation of Chehroudi et al. [11] were obtained considering the density spreading angle, whereas the centerline-velocity decay did not follow the pseudosimilarity laws of Chen and Rodi [20]. They also noticed that jets are surrounded by large density-gradient regions stabilizing the jet. LES has also been used for reactive cases in the SC regime: shear coaxial jet flames at SC pressure were investigated by Oefelein [21,22], Oefelein and Yang [3], Matsuyama et al. [23], and Tramecourt et al. [24].

In this study, two nitrogen jets at a SC pressure of 40 bar are considered. The pressure is kept constant for both cases, but the injection temperature varies: one is below the pseudo boiling temperature, whereas the other is slightly higher. As a consequence, departure from the perfect-gas behavior is limited in the second case, whereas the first case shows strong real-gas effects and density variations analogous to a continuous phase change. The main purpose of this paper is to evaluate how the LES equations, with standard low-pressure turbulence models, coupled with a real-gas equation of state compare with experiments. The behavior in the similarity region is studied and compared with the pseudosimilarity law of Chen and Rodi [20]. The present simulation is also compared with the LES of Zong [18], which is, to the authors knowledge, the only 3-D LES performed in a similar configuration and under SC conditions. Because of the scarcity of experimental measurement under supercritical conditions, our simulations will also be compared with a variety of variable-density low-pressure jets [25–30] in search for common features. This additional set of experimental data will be used for the analysis of the velocity field because velocity measurements under supercritical conditions are not available.

This paper is organized as follows. First, the real-gas model is presented and validated within the thermodynamic range of the study. Then the SC LES equations and subgrid-scale models are presented. Some considerations about the importance of the numerics are also discussed: the focus is set on the stabilization procedure needed to overcome the strong stratification observed at high pressure. Then the configuration, boundary conditions and mesh are described. Finally, the results are discussed and compared with available experimental data at both low and high pressures.

Real-Gas Model

In this section, two key ingredients for the numerical simulation of supercritical flows are presented: the EOS and the models for transport phenomena. The Peng–Robinson equation of state (PR EOS) was chosen for this work [31]:

$$P = \frac{\rho r T}{1 - \rho b} - \frac{\rho^2 a(T)}{1 + 2\rho b - \rho^2 b^2} \tag{1}$$

where P is the pressure, T is the temperature, ρ is the density, $r = R/W$ (with R being the perfect-gas constant), and W is the molar mass. The coefficients $a(T)$ and b are defined as

$$a(T) = 0.457236 \frac{(rT_c)^2}{P_c} \left[1 + c\left(1 - \sqrt{\frac{T}{T_c}}\right)\right]^2 \tag{2}$$

$$b = 0.077796 \frac{rT_c}{P_c} \tag{3}$$

where P_c is the critical pressure, T_c is the critical temperature, and the additional parameter c is defined as a function of the acentric factor ω by

$$c = 0.37464 + 1.54226\omega - 0.26992\omega^2 \tag{4}$$

Equation (1) is used for a consistent derivation of the pressure dependence of thermodynamic coefficients (heat capacities, compressibility, speed of sound, etc.), as presented by Miller et al. [32].

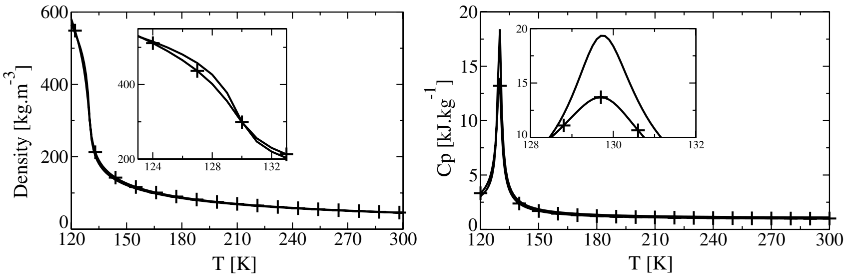

a) b)

Fig. 1 Validation of the EOS and thermodynamics for pure nitrogen: a) density and b) constant-pressure heat capacity; NIST database (solid line) and real-gas model (notched line), based on the PR EOS [31].

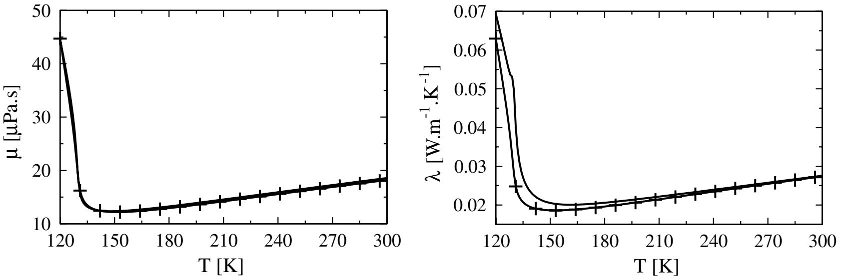

a) b)

Fig. 2 Transport coefficients of pure nitrogen: a) viscosity and b) thermal conductivity; NIST database (solid line) and Chung et al. [38] (notched line).

Finally, the low-pressure reference is provided by the JANAF thermodynamical tables [33].

The validity of this model for the present study is evaluated in Fig. 1 by comparing the density ρ and the constant-pressure heat capacity C_p with values from the NIST database.¶ For this validation, the pressure is set to 40 bars and the temperature varies from 120 to 300 K, which covers the experimental conditions for the two cases computed in this study. The relative error is less than 3% for the density and 10% for the heat capacity, except at the pseudo boiling line (cf. Fig. 1b around 130 K), where the error locally increases to 5% for the density and 20% for the heat capacity.

The adequate framework for the description of transport phenomena under supercritical conditions is that of the fluctuation/dissipation theory [34]. The formulation proposed by Miller et al. [35] and Harstad and Bellan [36,37] is consistent with the kinetic theory at low pressure and serves as a baseline for this study. For the particular conditions considered in this work, many simplifications can be made. Indeed, for single-species calculations, the only term that remains in the heat flux q is the classical Fickian contribution:

$$q_i = -\lambda \frac{\partial T}{\partial x_i} \tag{5}$$

where λ is the thermal conductivity. The method proposed by Chung et al. [38] is used to compute the transport coefficients: the thermal conductivity λ and the dynamic viscosity μ. These coefficients compare favorably with the NIST database in the range of thermodynamic conditions of this study (Fig. 2).

Altogether, this model provides a quantitative evaluation of thermodynamic variables over a wide range of pressure and temperature. Note that it naturally degenerates toward perfect-gas behavior when the pressure is decreased.

Governing Equations

One objective of this paper is to assess the performance of the LES methodology for the computation of supercritical turbulent flows. However, the derivation of the LES equations at high pressure is still an open subject with two major additional issues compared with low-pressure flows:

1) The validity of the existing subgrid-scale (SGS) models, developed for ideal gases, should be examined.

2) Additional SGS contributions may be necessary because of the nonlinearities in the EOS and the transport coefficients.

The a priori study of Selle et al. [13] suggests that existing SGS models perform similarly in perfect-gas and real-gas flows. However, the nonlinearity of the EOS, and to a lesser extent the transport models, seem to call for additional SGS contributions, but their exact structure and importance has not been determined yet. In addition, the strong density gradients encountered at high-pressure call for specific stabilization of the numerical schemes that is described in the following section.

Large-Eddy Simulation Equations

The primitive variables for the description of a single-species continuum (gaseous, liquid or supercritical fluid) are the density ρ, the velocity components u_i ($i \in [1,3]$), the pressure P and the temperature T. The total energy e_t is defined as $e_t = e + e_k$, where e is the internal energy and $e_k = u_i u_i/2$ is the kinetic energy. The vector of conservative variables is $\phi = (\rho, \rho u_i, \rho e_t)$. The methodology for deriving the LES equations is to apply a filtering operator, denoted as $\bar{\bullet}$, onto the set of conservation equations. Then the filtered conservative variables vector is $\bar{\phi} = (\bar{\rho}, \overline{\rho u_i}, \overline{\rho e_t})$, which can also be written in terms of Favre-averaged variables: $\bar{\phi} = (\bar{\rho}, \bar{\rho}\tilde{u}_i, \bar{\rho}\tilde{e}_t)$. The set of LES equations for single-species SC fluids used in this work is

$$\frac{\partial \bar{\rho}}{\partial t} + \frac{\partial \bar{\rho}\tilde{u}_j}{\partial x_j} = 0 \tag{6}$$

$$\frac{\partial \bar{\rho}\tilde{u}_i}{\partial t} + \frac{\partial \bar{\rho}\tilde{u}_i\tilde{u}_j}{\partial x_j} = -\frac{\partial P(\bar{\phi})}{\partial x_i} + \frac{\partial \sigma_{ij}(\bar{\phi})}{\partial x_j} - \frac{\partial \bar{\rho}\tau_{ij}}{\partial x_j} \tag{7}$$

$$\frac{\partial \bar{\rho}\tilde{e}_t}{\partial t} + \frac{\partial \bar{\rho}\tilde{e}_t\tilde{u}_j}{\partial x_j} = -\frac{\partial P(\bar{\phi})\tilde{u}_j}{\partial x_j} - \frac{\partial q_j(\bar{\phi})}{\partial x_j} + \frac{\partial \sigma_{ij}(\bar{\phi})\tilde{u}_i}{\partial \partial x_j} - \frac{\partial \bar{\rho}\zeta_j}{\partial x_j} \tag{8}$$

[¶] Data available online at http://webbook.nist.gov [retrieved March 2010].

where σ is the viscous-stress tensor:

$$\sigma_{ij} = 2\mu\left(S_{ij} - \frac{1}{3}S_{kk}\delta_{ij}\right) \tag{9}$$

$$S_{ij} = \frac{1}{2}\left(\frac{\partial u_i}{\partial x_j} + \frac{\partial u_j}{\partial x_i}\right) \tag{10}$$

and the SGS contributions τ and ζ are defined as

$$\tau_{ij} = \widetilde{u_i u_j} - \tilde{u}_i\tilde{u}_j \tag{11}$$

$$\zeta_j = \widetilde{hu_j} - \tilde{h}\tilde{u}_j \tag{12}$$

The notation $P(\bar{\phi})$ [respectively, $q_j(\bar{\phi})$ and $\sigma_{ij}(\bar{\phi})$] means that the functional form of Eq. (1) [respectively, Eqs. (5) and (9)] is used together with the vector of filtered variables $\bar{\phi}$. In general, the filtered function $\overline{\psi(\phi)}$ and the function computed on the filtered field $\psi(\bar{\phi})$ are not equal, unless ψ is a linear function.

Equations (6–8) are based on the derivation of Selle et al. [13] (their Eqs. 4.6 to 4.8) with additional simplifications. First, the term $\partial\bar{\rho}\tau_{ij}\tilde{u}_i/\partial x_j$ in their Eq. 4.8 is shown [13] to be at least 1 order of magnitude smaller than the other resolved terms, so that it is neglected. Then in the case of single-species flows, the heat flux is mildly nonlinear because only the Fickian term is present so that the approximation $\overline{q_j(\phi)} = q_j(\bar{\phi})$ is retained. Last but not least, because the EOS is a nonlinear function of the primitive variables [cf. Equations (1–3)] the application of the LES filter will yield subgrid-scale contributions. This question is discussed at length by Selle et al. [13] who proposed a model for the filtered pressure $\bar{P}$. However, as a first step for this study, the approximation $\bar{P} = P(\bar{\phi})$ is retained.

Subgrid-Scale Models and Assumptions

The closure of the Reynolds stresses [Eq. (11)] requires particular attention. For the LES of jets, the subgrid-scale model should be able to limit dissipation in the pure shear zone, where the linear perturbations grow before transition to turbulence. For such configuration, the classical Smagorinsky model is known to be too dissipative and the wall-adapting local eddy-viscosity model [39] [Eq. (14)], which has been designed to be less dissipative in pure shear zones by accounting for the rotational rate, is used. The SGS stress tensor is then

$$\tau_{ij} = 2\nu^t\left(\tilde{S}_{ij} - \frac{1}{3}\delta_{ij}\tilde{S}_{ll}\right) \tag{13}$$

with

$$\nu^t = (C_w\Delta)^2\frac{(s^d_{ij}s^d_{ij})^{3/2}}{(\tilde{S}_{ij}\tilde{S}_{ij})^{5/2} + (s^d_{ij}s^d_{ij})^{5/4}} \tag{14}$$

$$s^d_{ij} = \tfrac{1}{2}(\tilde{g}^2_{ij} + \tilde{g}^2_{ji}) - \tfrac{1}{3}\tilde{g}^2_{kk}\delta_{ij} \tag{15}$$

where $C_w = 0.4929$, Δ is the filter size and $\tilde{g}_{ij}$ is the velocity-gradient tensor :

$$\tilde{g}_{ij} = \frac{\partial\tilde{u}_i}{\partial x_j} \quad \text{and} \quad \tilde{g}^2_{ij} = \tilde{g}_{ik}\tilde{g}_{kj} \tag{16}$$

The SGS energy flux [Eq. (12)] is modeled using the gradient transport assumption:

$$\bar{\rho}\zeta_j = -\frac{\mu_t\bar{C}_p}{Pr^t}\frac{\partial\tilde{T}}{\partial x_i} \tag{17}$$

where μ_t is the turbulent viscosity and Pr^t is the turbulent Prandtl number. Following previous work [40], the value $Pr^t = 0.6$ is used.

Numerics

The AVBP [41] code used for this study solves the compressible Navier–Stokes equations for a multicomponent mixture of fluids on unstructured meshes. To achieve high-quality LES, a widespread approach is to use high-order low-dissipation centered schemes [42,43]. For example, the two-step Taylor–Galerkin–Colin (TTGC) scheme [44] implemented in AVBP is third-order in time and space has successfully been validated for both nonreacting and reacting flows [45]. For SC flows, however, very steep density gradients are often present so that the numerics had to be adapted to avoid spurious oscillations. Because the purpose of this paper is not the description of the cell-vertex formalism used in AVBP [41,44] the focus is set on the specific adaptations for SC flows rather than an extensive description of the discrete expressions for the operators. The strategy that was chosen is to use artificial viscosity (as, for example, proposed by Jameson et al. [46]), and it can be decomposed in three parts:

1) The variables that need stabilization are identified. For low-pressure nonreacting LES the stabilization of the momentum equation is sufficient. For reacting flows the energy equation needs stabilization. However, under SC conditions, the density field also had to be stabilized.

2) A function $\zeta_{k,j}$ is devised to detect underresolved gradients at node k in cell Ω_j:

$$\zeta_{k,j} = \frac{|\rho_{\Omega_j} - \rho_k - (\nabla\rho)_k.(\boldsymbol{x}_{\Omega_j} - \boldsymbol{x}_k)|}{|\rho_{\Omega_j} - \rho_k| + |(\nabla\rho)_k.(\boldsymbol{x}_{\Omega_j} - \boldsymbol{x}_k)| + |\rho^{\mathrm{PG}}_k|} \tag{18}$$

where ρ_k (respectively, ρ_{Ω_j}) is the density at node k (respectively, in cell Ω_j), and $\rho^{\mathrm{PG}}_k = P/(rT)$ is the perfect-gas approximation of the density. The sensor ξ_{Ω_j} is then defined as

$$\xi_{\Omega_j} = \frac{1}{2}\left(\tanh\left(\frac{\psi - \psi_0}{\delta}\right) - \tanh\left(\frac{-\psi_0}{\delta}\right)\right) \tag{19}$$

where $\psi = \max_{k\in\Omega_j}(0, \zeta_{k,j})$ and the model constants ψ_0 and δ are set to 0.2 and 0.05, respectively.

3) A blend of contributions from two operators is added to the solution. A second-order derivative is used to add viscosity when the sensor is activated: this smoothes the largest gradients. A fourth-order derivative is also added to avoid node-to-node oscillations outside the gradients [44]. The coefficients for these two contributions are set to the lowest value, preserving monotonicity.

One peculiarity of SC flows is the highly nonlinear thermodynamics, consequently, if the artificial dissipation is not applied consistently on all variables, it can perturb the pressure field and generate strong acoustic waves. The minimization of this unphysical noise was achieved by writing the exact differential of pressure with respect to total energy ρe_t, density, and momentum:

$$dP = \frac{\alpha}{\rho\beta C_v}d(\rho e_t) + \frac{C_p - \alpha h + \alpha e_k}{\rho C_v\beta}d\rho - \frac{\alpha u_i}{\beta\rho C_v}d(\rho u_i) \tag{20}$$

where α is the thermal expansion coefficient, β is the isothermal compressibility coefficient, C_p and C_v are the heat capacities, h is the enthalpy (per mass unit), and e_k is the kinetic energy. Imposing $dP = 0$ in Eq. (20) allows to construct the variation of ρe_t, consistent with the modification of ρ and ρu_i by artificial viscosity, that does not generate pressure fluctuations.

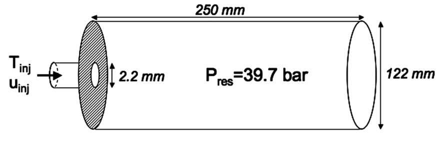

Fig. 3 Sketch of the configuration.

Table 1 Operating conditions for cases 3 and 4 of Mayer et al. [15]

Case	T_{inj}, K	u_{inj}, m.s^{-1}	T/T^{pb}	$\rho_{\mathrm{inj}}/\rho_{\infty}$	Re_{inj}
3	126.9	4.9	0.98	9.6	1.7×10^5
4	137	5.4	1.06	3.7	1.6×10^5

Finally, the boundary conditions are treated with the characteristic wave decomposition method NSCBC (Navier–Stokes characteristic boundary conditions) [41,47], which was also adapted to real-gas thermodynamics [48].

Flow Configuration

The configuration is the experimental setup of Mayer et al. [15]. It consists of a single round jet (diameter 2.2 mm) injected in a cylindrical chamber (diameter 122 mm) pressurized at 39.7 bar at a temperature of 298 K (Fig. 3). The critical-point coordinates of nitrogen are $P_c = 33.958$ bar and $T_c = 126.192$ K so that the setup is under supercritical conditions.

Thermodynamic Conditions

Two cases with a different inlet temperature were computed and are presented in Table 1. These cases are numbered according to Mayer et al. [15] and were chosen because they are particularly challenging for a numerical solver. Indeed, for such single-species flows, the proximity of the critical point (jet reduced temperature $1.006 < T_r < 1.086$ and reduced pressure $P_r = 1.17$) represents a worst-case scenario in terms of thermodynamic properties and density variations (cf. Fig. 4) [9,49]. The density ratio is $\rho_{\mathrm{inj}}/\rho_{\infty} = 9.6$ for case 3 ($\rho_{\mathrm{inj},3} = 435\ \mathrm{kg \cdot m^{-3}}$) and $\rho_{\mathrm{inj}}/\rho_{\infty} = 3.7$ for case 4 ($\rho_{\mathrm{inj},4} = 171\ \mathrm{kg \cdot m^{-3}}$). Moreover, despite the relatively small temperature difference between the two cases, the fact that the pseudo boiling temperature ($T^{\mathrm{pb}} = 129.5$ K at 39.7 bar) lies just between cases 3 and 4 dictates qualitatively different behaviors. The pseudo boiling temperature T^{pb} is the temperature for which, at a given pressure, the constant-pressure heat capacity C_p reaches its maximum; it is the prolongation of the gas/liquid phase-change line. Consequently, whereas for case 3, C_p initially increases when the jet heats up, it monotonically decreases for case 4, as shown in Fig. 4b. Note, however, that because of the strong changes in dynamic viscosity near the pseudo boiling temperature (Fig. 2), the Reynolds numbers at injection for cases 3 and 4 are very close: $Re_{\mathrm{inj}} \sim 160,000$.

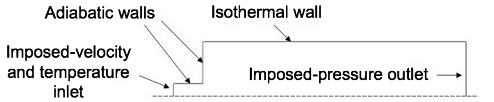

Fig. 6 Sketch of the boundary conditions used in the present simulation.

Numerical Setup: Mesh and Boundary Conditions

The computational domain is presented in Fig. 5a, and a longitudinal cut of the mesh is displayed in Fig. 5b. This fully unstructured grid (tetrahedral cells) is finest near the injector, with a constant characteristic cell size of $\Delta = 0.1$ mm in a cylinder of diameter 1.8 times the jet diameter and length almost 10 diameters. This zone is followed by a smoothly coarsening region. The mesh, which is the same for both cases, contains 9.4×10^5 points and 5.5×10^6 tetrahedra.

The boundary conditions are presented in Fig. 6. The pressure in the reservoir is maintained by a nonreflecting outlet relaxed to a target pressure [48]. The walls near the injector are treated as adiabatic, whereas the reservoir walls are kept at a constant temperature of 298 K. The velocity and temperature are imposed at the inlet with turbulent perturbations prescribed by the procedure initially developed by Kraichnan [50] and Smirnov et al. [51]. No measurement of the velocity fluctuation level are provided at the injector exit, thus an intensity of 2.5% of the mean flow is imposed, which is a typical value for turbulent round jets. A sensitivity study was performed on a coarse mesh (Table 2) for case 3 with a turbulence level of 5% instead of 2.5%. The following procedure was used: once the computation has reached a statistically stationary state at a 2.5% turbulence level, an instantaneous solution is chosen as initial condition for the analysis. From this solution, averaging is performed over 0.03 s at 2.5% turbulence and an other computation at 5% turbulence is ran for 0.01 s (without averaging) and then averaged over 0.03 s. This averaging time is sufficient for the analysis, as it corresponds to three convection times over 22 diameters at u_{inj}. The normalized centerline density ρ^* [cf. Equation (22)] is presented in Fig. 7a for both turbulence levels. It shows that the dense-core length is shortened at the higher inlet turbulence, but past the transition region, the solutions have the same evolution. The analysis of density

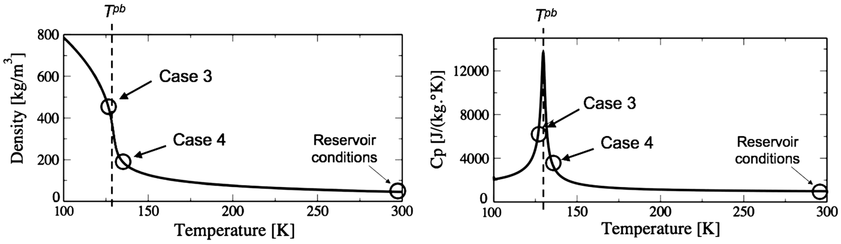

a) b)

Fig. 4 Plots of a) density and b) heat capacity for cases 3 and 4; jet and reservoir conditions (○).

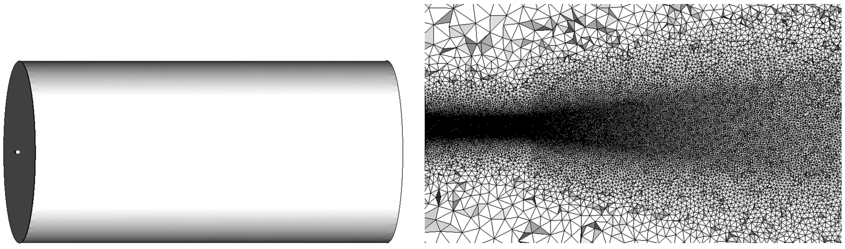

a) b)

Fig. 5 Sketches of a) view of the computational domain and b) cut of the mesh on a length of 30 injector diameters.

Table 2 Summary of meshes characteristics

Mesh name	Δ, mm	No. of points	No. of cells
Coarse	0.133	4.1×10^5	2.4×10^6
Intermediate	0.100	9.4×10^5	5.5×10^6
Fine	0.075	2.2×10^6	13.7×10^6

Table 3 Information about the time-averaging procedure and high-performance computing for the different meshes and cases

Case and mesh	Δt, μs	T_{aver}, s[a]	T_{aver}/τ_c	No. of CPUs times wall clock, h
3 coarse	0.110	0.143	6.4	128×60
3 intermediate	0.070	0.161	7.2	512×107
3 fine	0.045	0.045	2	1024×50
4 intermediate	0.070	0.140	6.8	512×91

[a] The number of flow-throughs during the averaging procedure (T_{aver}) is based on the reference convective time $\tau_c = 50d/u_{\mathrm{inj}}$.

fluctuations [cf. Equation (25)] in Fig. 7b yields the same conclusion, as both inlet turbulence values reach the same fluctuation levels.

For the computation of both case 3 and 4, the fluid is initially at rest and at reservoir temperature. The calculations are first computed on a coarse mesh (cf. the convergence study detailed below) and then interpolated on finer meshes. The computations are basically never restarted from the initial condition during the whole process of fine tuning of numerical parameters (we first use a fast second-order Lax–Wendroff scheme and then switch to the more precise third-order scheme called TTGC [44]) and the averaging of the flow is started only after domain-averaged quantities (mass fluxes, pressure, resolved kinetic energy, etc.) reach a steady state.

A mesh-convergence study was carried out to assess the accuracy of the simulation on our grid. The computation of case 3 was carried out on a coarser and finer mesh whose characteristics are summarized in Table 2. Between the coarse and fine meshes, there is almost a factor of 2 for the cell size Δ in the refined region (ten diameters downstream of the injection). Table 3 presents the characteristics of all the computations: case 3 on the three meshes and case 4 on the intermediate mesh. The results of the convergence study are summarized in Fig. 8, in which the time-averaged centerline-density profile is plotted for the three meshes. First, the dense-core length (i.e., the initial density plateau) is slightly longer for the coarse mesh but virtually identical for the intermediate and fine meshes. In the region where the density varies the most (i.e., between $x/d = 20$ and 30), the averaged density with the coarse mesh is significantly higher, whereas the intermediate and fine meshes predict marginally different values. The results of Fig. 8 indicate that the intermediate mesh offers the best precision over computational-cost ratio, and it was therefore chosen for this study. All results presented in the remainder of the paper were obtained on the intermediate mesh.

Results and Discussion

Flow Visualization

An instantaneous isocontour of density $\rho_{0.5} = (\rho_{\mathrm{inj}} + \rho_\infty)/2$ is presented in Fig. 9. For both cases, the development of coherent structures on the outer side of the jet eventually leads to complete destabilization, transition to turbulence and mixing of the jet with the ambient fluid. As presented in Table 1, the jet density for case 3 is much larger than for case 4. Consequently, case 3 has a much longer dense core, together with the intermittent emission of dense pockets, which are resilient to destruction by turbulence. Overall, the larger density difference seems to hinder the development of turbulence, together with a lower mixing efficiency. From a thermodynamics perspective, the resistance of case 3 to heat transfer can also be attributed to the surge of C_p across the pseudo boiling line (cf. Fig. 4b).

To reconstruct shadowgraphlike images, Fig. 10 (bottom) shows the integration of the density gradient along the line of sight. The same visual characteristics as in Mayer et al. [15] (Fig. 10, top), are present. First, both jets are initially surrounded by large density gradients, much larger for case 3. The dense-core lengths are in qualitatively good agreement, this point will be quantified. Stretched entities emerging from the central core are visible in case 3 for both numerical and experimental results. Finally, in both experiment and simulation, strong density gradients are still present at the end of the visualization region for case 3, whereas they quickly fade out in case 4.

Normalized Centerline Profiles

The centerline profile of density was measured by Mayer et al. [15] using 2-D Raman technique. These results are compared with the

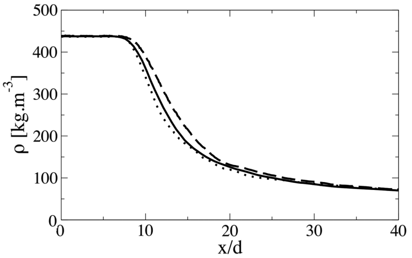

Fig. 8 Centerline-density profile: mesh-convergence study; coarse mesh (dashed line), intermediate mesh (solid line) and fine mesh (dotted line).

Fig. 9 Isocontour of density $\rho_{0.5} = (\rho_{\mathrm{inj}} + \rho_\infty)/2$ in the near injector zone (20 diameters).

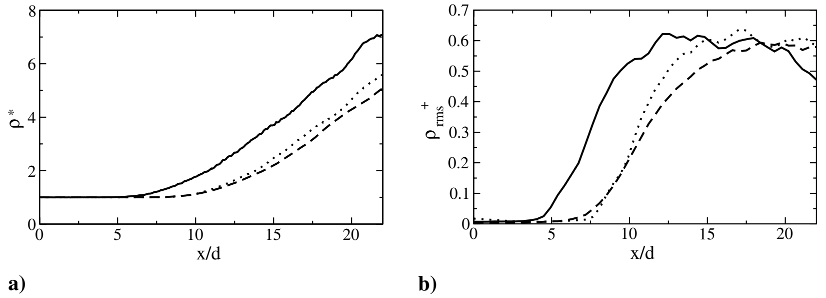

a) b)

Fig. 7 Sensitivity study of the turbulence level prescribed at the inlet: a) normalized centerline density [cf. Equation (22)] and b) centerline-density fluctuations [cf. Equation (25)]; 2.5% turbulence (dashed line), 5% turbulence (solid line), and 5% translated to account for the reduction of the dense core (dotted line).

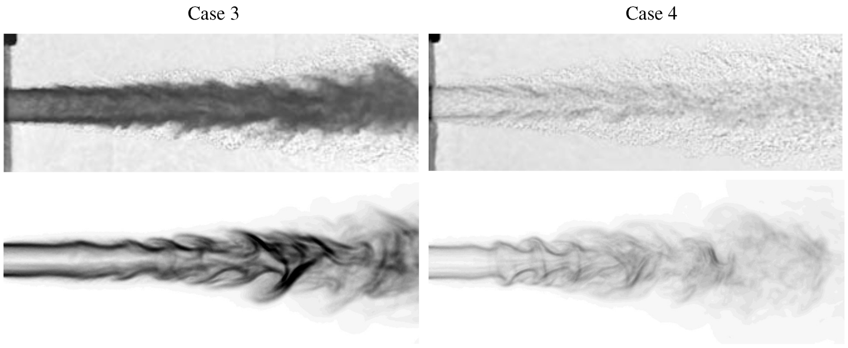

Fig. 10 Shadowgraphs from Mayer et al. [15] for cases 3 and 4 (top) and numerically reconstructed shadowgraphs of cases 3 and 4 (bottom) over a distance of 12 injector diameters.

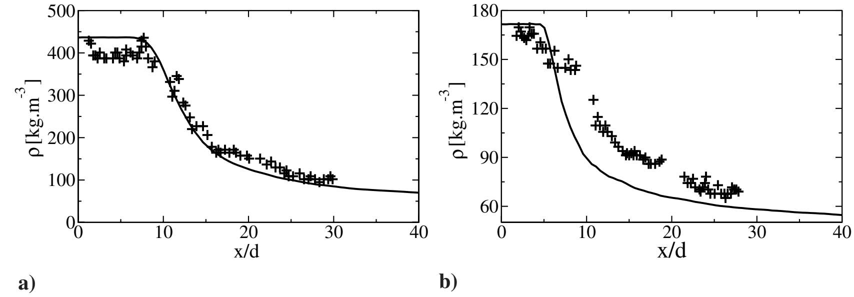

Fig. 11 Comparison between experimental results and LES results of the Centerline density in terms of normalized distance from the injector: a) case 3 and b) case 4; present LES (solid line) and + Mayer et al. [15] (notched line).

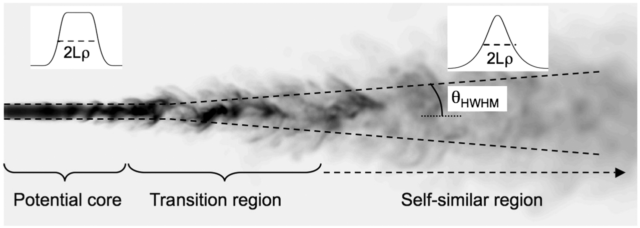

Fig. 12 Schematic representation of the determination of the HWHM spreading angle θ^H using the density field (from Raman spectroscopy in the experiments).

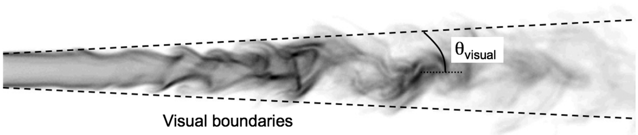

Fig. 13 Principle of the determination of the visual spreading angle θ^V of the jet (from shadowgraph images in experiments).

present numerical simulations in Fig. 11 and show good agreement. For case 3, the computational results accurately predict the drop in centerline density despite a small (∼10%) overestimation near the injector, which could be due to a systematic error of the Raman technique in very-high-density regions [15]. For case 4, however, there are large discrepancies, one striking feature of the experimental data being the absence of an identifiable dense-core region near the injector, which is not consistent with the visualizations. It is therefore

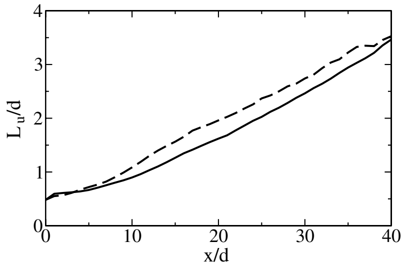

Fig. 15 HWHM of the velocity L_u as a function of the distance from the injector x/d; case 3 (solid line) and case 4 (dashed line).

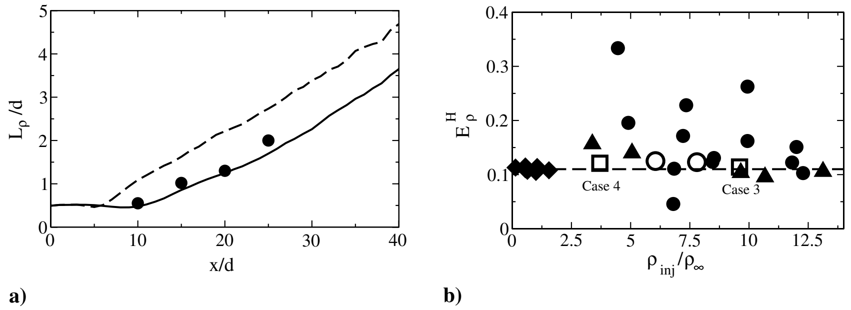

Fig. 14 Plots of a) evolution of jet HWHM L_ρ downstream of the injector; Mayer et al. [15] for case 3 (●); present LES for case 3 (solid line) and for case 4 (dashed line), and b) HWHM density spreading rate E^H_ρ: Mayer et al. [15] (●), Oschwald and Micci [16] (▲), Richard and Pitts [27] (◆) (low-pressure experiment), Chen and Rodi [20] (dashed line) (0.11), real-gas simulations of Zong [18] (○), and present simulations (□).

Table 4 Spreading rates of velocity E_u in terms of density ratio and comparison with other available data for variable-density jets from the literature [25,28–30]

$\rho_{\mathrm{inj}}/\rho_\infty$	0.14 [28,29]	1 [25,28–30]	1.54 [25]	3.7 [a]	9.6 [a]
E_u	0.109–0.110	0.088–0.096	0.085	0.080	0.090

[a] Present simulations.

difficult to draw a definite conclusion on this comparison. From the centerline-density profiles, one can evaluate the dense-core length, which is defined as the downstream coordinate where the density decreases below 99% of ρ_{inj}. It is found to be 7.9 diameters for case 3 and reduces to 5.1 diameters for case 4.

Spreading Rates

The spreading rate of a jet is a direct measure of mixing efficiency. In this section, the spreading rates of the jet are evaluated using either the density or the velocity fields.

Using the density field, two criteria based on available experimental results can be derived. The first criterion is called the half-width, half-maximum (HWHM) [10,14] and is illustrated in Fig. 12. Cross-stream profiles of average density are used to define the half-width L_ρ of the jet, taken at the median value between dense and light regions. Then the spreading rate E_ρ^H is defined as the slope of the linear regression of L_ρ along the jet axis. For consistency, the linear regression must be performed in a region where L_ρ increases linearly, which is typically the case past the dense-core and transition zone. The HWHM spreading angle θ^H is then defined as

$$\theta^H = \arctan(E_\rho^H) \tag{21}$$

The second criterion for the density spreading rate is based on a direct visualization of the flow, for example, by drawing the outermost observable extent of the jet from a shadowgraph image [11]. The principle of this method is presented in Fig. 13. Obviously, the two measures θ^H and θ^V are expected to differ for at least one reason: θ^H does not account for the initial dense-core region of the jet, whereas θ^V does. However, it was suggested [11] that the two would be related through a simple factor of 2. Evaluating the visual extent of the jet from a time-averaged density field obtained by numerical simulation is a difficult task, as it is very sensitive to the threshold for density. This quantity is therefore not presented in the present analysis, although it is an appropriate experimental measurement.

The HWHM methodology can be duplicated to measure the half-width of the velocity profile at half the maximum L_u and derive the velocity spreading rate E_u^H through linear regression.

Density Spreading Rate

The jet HWHM L_ρ is presented in Fig. 14a for the LES of cases 3 and 4 as well as the experimental results of Mayer et al. [15] for case 3. First, one can note that the jet initially keeps a constant width followed by a linear increase, a feature that was also experimentally observed [16]. Then for case 3, the LES matches the experimental measurements, which is consistent with the jet-axis density profiles presented in Fig. 11. This means that for case 3, which crosses the pseudo boiling point and has the most real-gas effects, the LES predictions quantitatively agree with the experiment in terms of jet length and width.

In Fig. 14b the spreading rate E_ρ^H of the present simulations are compared with experimental data (both low- and high-pressure), semi-empirical analysis [20] as well as existing numerical simulations [18]. For the present simulations, the computation of E_ρ^H is based on a linear regression of L_ρ for $15 < x/d < 50$. The first striking feature is that the measurements of Mayer et al. [15] are extremely scattered even for a fixed density ratio (e.g., $\rho_{\mathrm{inj}}/\rho_\infty \sim 10$ in Fig. 14b), which is quite strange given the agreement on L_ρ. At present, there is no explanation for this discrepancy. Our simulations are, however, in very good agreement with the measurements of Oschwald et al. [9,16] despite a slight underestimation for case 4 ($\rho_{\mathrm{inj}}/\rho_\infty \sim 3.7$ in Fig. 14b). The last set of experimental results reported in Fig. 14b is the low-pressure data of Richard and Pitts [27], which cover density ratios lower than 2. With the notable exception of the results from Mayer et al. [15], both experiments and simulations suggest that the density ratio has a very limited impact on the spreading rate of the jet. It is also evident that all of these data are quite consistent with the semi-empirical formulation proposed by Chen and Rodi [20] stating that $E_\rho^H \sim 0.11$.

Velocity Spreading Rate

Duplicating the same methodology, the HWHM of the velocity field L_u is presented in Fig. 15. It is interesting to note that the initial plateau observed on L_ρ in Fig. 14a is not present on the velocity field. Low-density-ratio experiments show such a plateau, with one notable exception in the experiment of Amielh et al. [29], in which $\rho_{\mathrm{inj}}/\rho_\infty = 0.14$: L_u initially decreases downstream of the injector and eventually linearly increases (Fig. 6 in [29]). It is also observed that past a transition region (typically $x/d > 10$) both jets show a linear evolution of L_ρ and L_u, which can be considered as an a posteriori justification for the computation of the spreading rates through linear regression.

The velocity spreading rate E_u of the present simulations is compared with available experimental data. Unfortunately, the

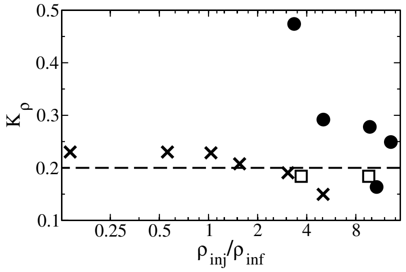

Fig. 17 Density decay coefficient K_ρ; Chen and Rodi (0.2) (dashed line), present simulations (□), Oschwald and Micci [16] (Raman) (●), and Pitts [26] (low-pressure measurements) (×).

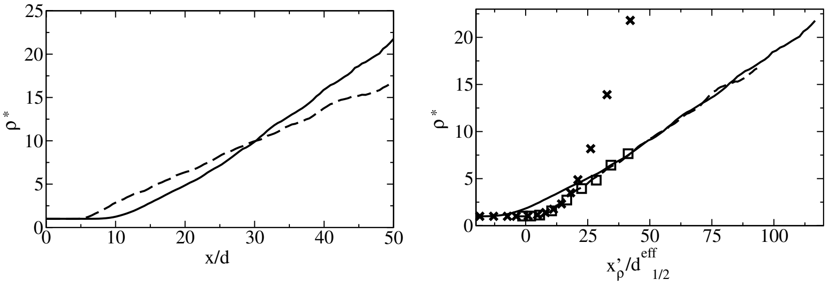

a) b)

Fig. 16 Plots of a) normalized density ρ^* [Eq. (22)] along the jet centerline and b) ρ^* with downstream coordinate normalized by the effective diameter $d_{1/2}^{\mathrm{eff}}$ [Eq. (24)]; case 3 (solid line), case 4 (dashed line), real-gas LES results for $\rho_{\mathrm{inj}}/\rho_\infty = 7.9$: Zong [18] (×), and low pressure $\rho_{\mathrm{inj}}/\rho_\infty = 1.43$: Chassaing [25] (□) .

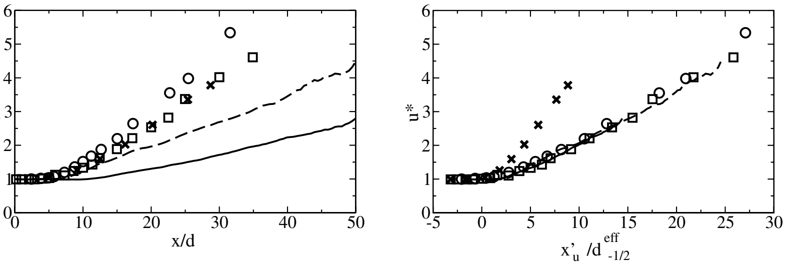

a) b)

Fig. 18 Plots of a) normalized velocity u^* [Eq. (23)] along the jet centerline and b) centerline u^* with downstream coordinate normalized by the effective diameter $d^{\mathrm{eff}}_{-1/2}$ [Eq. (24)]; case 3 (solid line), case 4 (dashed line). $\rho_{\mathrm{inj}}/\rho_\infty = 1.43$: Chassaing [25] (□), $\rho_{\mathrm{inj}}/\rho_\infty = 1$: Chassaing [25] (○), and real-gas LES results for $\rho_{\mathrm{inj}}/\rho_\infty = 7.9$: Zong [18] (×).

measurement of velocity fields in high-pressure flows is a practical challenge so that the velocity spreading rates are not available from Mayer et al. [15]. Consequently, other variable-density low-pressure round-jet experiments are considered for comparison [25,28–30]. These results are summarized in Table 4. Overall, the velocity spreading rate is weakly affected by the density ratio, especially for $\rho_{\mathrm{inj}}/\rho_\infty \geq 1$. On the other hand, for the lower $\rho_{\mathrm{inj}}/\rho_\infty$, the spreading rate is enhanced by around 20%. This could be attributed to buoyancy effects, which were not taken into account in our simulations: Amielh et al. [29] pointed out that E_u can be significantly influenced by confinement effects induced by walls or coflow, which was not tested in this work.

Pseudosimilarity Analysis

The centerline density and velocity fields are normalized in search for similarity among supercritical jets. Common definitions for variable-density jets are

$$\rho^* = \frac{\rho_{\mathrm{inj}} - \rho_\infty}{\rho - \rho_\infty} \tag{22}$$

$$u^* = \frac{u_{\mathrm{inj}}}{u} \tag{23}$$

noting that ρ^* (respectively, u^*) is actually inversely proportional to the density (respectively, the velocity). It is well known that variable-density jets are not similar when the coordinates are normalized by the jet diameter. This observation also holds for supercritical jets, as shown in Fig. 16a. However, past the initial dense-core region where the density is constant, ρ^* follows a linear evolution for both cases. It was first proposed by Thring and Newby [52] that the normalization of the downstream coordinate uses an effective diameter d^{eff}_α, depending on the density ratio and defined as

$$d^{\mathrm{eff}}_\alpha = d\left(\frac{\rho_\infty}{\rho_{\mathrm{inj}}}\right)^\alpha \tag{24}$$

For low-pressure variable-density jet, the centerline evolutions of ρ^* (respectively, u^*) collapse onto a single line in the region where the jet is fully developed [28,29] for $\alpha = 1/2$ (respectively, $\alpha = -1/2$). In Fig. 16b the downstream coordinate is now normalized by $d^{\mathrm{eff}}_{1/2}$, but each curve is also horizontally translated by a different value to account for the changes in dense-core and transition regions lengths. The resulting shifted coordinate is denoted as x'. Figure 16b shows that the two supercritical jets considered in this paper now have the same slope in the fully developed region. Note that the transition region seems to be affected by the large density ratio of case 3. It is interesting to see that in comparison with the low-pressure jet of Chassaing [25], similar behaviors are once again observed, even in the transition zone for case 4. The collapsing of all curves past the transition region may not be so surprising as the cold jet gradually heats up toward the chamber's conditions. Indeed, in the thermodynamic conditions of the chamber (298 K and 39.7 bar) the compressibility factor $Z = P/(\rho r T)$, which is a measure of the departure from the perfect-gas EOS is $Z = 0.996$. This would explain how, once the jet has transitioned and turbulent mixing is efficient, these SC jets behave like low-pressure jets. Finally, the LES results of Zong [18] also reported in Fig. 16b exhibit a drastically different behavior and does not seem to agree with the experimental data from Mayer et al. [15] (Fig. 11). At present, there is no explanation for such discrepancy.

The slope of ρ^*, denoted as K_ρ, is presented in Fig. 17 for experimental configurations at both low and high pressure. Once again, high-pressure Raman measurements [16] are quite widely scattered whereas the present computations show virtually no influence of the density ratio. Once again, it appears that the supercritical jets favorably compare with low-pressure experiments [26].

The normalized velocity u^* is compared with experimental data from Chassaing [25] as well as the real-gas simulation of Zong [18]. Figure 18a presents the centerline evolution of u^* and, consistently with low-pressure experiments, it appears that lighter jets show a faster velocity decay [29]. One notable exception is the real-gas simulation of Zong [18], which shows a velocity decay similar to the experiment of Chassaing [25] despite a much larger density ratio. Similarly to what was done for the density measurements, the downstream coordinate is normalized by $d^{\mathrm{eff}}_{-1/2}$ and Fig. 18b shows that the two present supercritical LES cases collapse onto experimental curves. Just like for the density ρ^*, the normalization by an effective diameter reveals a similarity between variable-density jets at both low and high pressure. Once again, the simulations of Zong [18] stand out by showing a much accelerated rate of decay for u^*.

The slope of u^* in the linear zone is noted K_u and is reported in Table 5 for a wide range of density ratios. Velocity-decay slopes show limited scattering with no clear trend as to the influence of the density ratio. Thermodynamic conditions also seem to have a marginal

Table 5 Velocity-decay constant K_u in terms of density ratio and comparison with other available data for variable-density jet from literature [25,28,30]

$\rho_{\mathrm{inj}}/\rho_\infty$	0.14 [28]	1 [25,28,30]	1.43 [25]	3.7 [a]	9.6 [a]
K_u	0.153	0.165–0.193	0.183	0.160	0.150

[a] Present simulation.

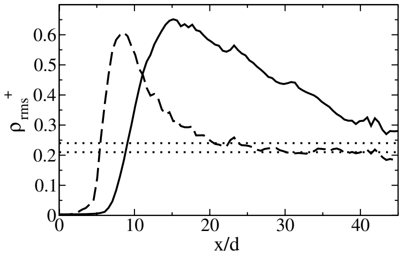

Fig. 19 RMS of centerline-density fluctuations, case 3 (solid line), case 4 (dashed line), and asymptotic range suggested by Chen and Rodi [20] (dotted line).

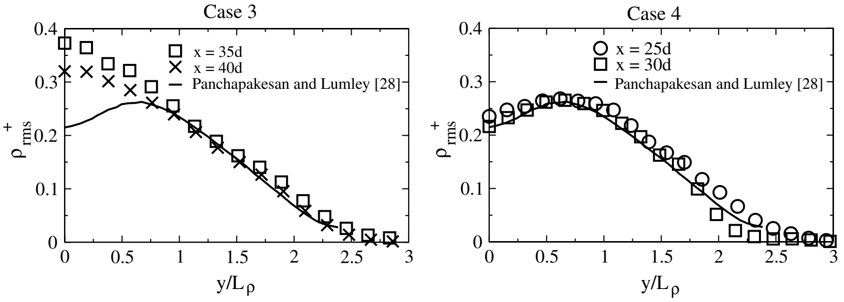

a) **b)**

Fig. 20 Radial profiles of the rms of $\rho^{+\prime}$ and comparison with passive-scalar rms in a low-pressure experiment [28].

impact, with, for example, the two extreme cases being as close as 2% in terms of K_u.

Density Fluctuations

The density fluctuation levels are scrutinized for both cases along the centerline of the jet and in the radial direction. To compare density fluctuations with available measurements of passive scalars, one defines ρ^+ as

$$\rho^+ = \frac{\rho - \rho_\infty}{\rho_c - \rho_\infty} \tag{25}$$

where ρ_c is the time-averaged centerline density. Figure 19 presents the root-mean-square fluctuations of ρ^+. Both cases show similar trends with an initial region void of fluctuations followed by a steep increase and a gradual decrease toward a plateau. The initial region is longer for case 3, which is consistent with the longer dense core. Both cases reach comparable fluctuation levels with a delayed peak for the dense case. In the decrease zone, the two cases differ notably, as case 4 shows a fast decrease (roughly inversely proportional to x) toward an asymptotic value, whereas for case 3 the fluctuations diminish approximately linearly. For case 4 the rms fluctuations of ρ^+ reach a plateau in the range proposed by Chen and Rodi [20] for passive-scalar fluctuations in low-pressure jets. Finally, the dense case also seems to stabilize in the same range despite the poor convergence of the rms, which could not be achieved so far downstream, mainly because of the mesh coarsening.

Additionally, radial profiles of the rms of ρ^+ are compared with the low-pressure experiment of Panchapakesan and Lumley [28] in Fig. 20. For case 4, which is the lighter jet, radial profiles at $x/d = 25$ and $x/d = 30$ are already self-similar and compare favorably with the experimental results. For case 3, however, (Fig. 20a), the density fluctuations at $x/d = 40$ are still significantly greater than in the low-pressure experiment. This is consistent with the visualization of dense pockets far downstream as well as the measurements presented in Fig. 19. However, in the outer skirt of the jet (typically $y/L_\rho > 1$) the supercritical jets match the low-pressure measurements of Panchapakesan and Lumley [28] ($\rho_{\mathrm{inj}}/\rho_\infty = 0.14$).

Conclusions

The simulation of two single-species round jets at supercritical pressure is achieved using the LES solver AVBP. Under such conditions, both jets exhibit departure from the perfect-gas behavior, which is accounted for by the use of the Peng–Robinson equation of state, consistent thermodynamics, and appropriate transport coefficients.

Along the initial mixing layer, the jets are characterized by the presence of strong density gradient, caused by the high density ratio between injection and reservoir conditions ($\rho_{\mathrm{inj}}/\rho_\infty = 3.7$ and 9.6). Although such conditions may call for the use of a modified subgrid-scale model, the present study uses standard low-pressure closure that neglects the unresolved nonlinearities due to the EOS. Despite this simplified approach, quantitative comparison of density fields and density spreading rates with high-pressure experimental data shows good agreement for the dense case, which has the most real-gas effects. These results suggest that the approach used in this study allows LES to obtain reasonable agreement considering the main features of highly real-gas single-species flows. Nevertheless, some unexpected discrepancies remain for the lighter case, mainly related to a scattering in the experimental data.

The spreading rates for density and velocity for both cases were compared with a large database of low- and high-pressure variable-density jets, pointing out little impact of the initial density ratio and thermodynamic conditions. The same observation holds for the pseudosimilarity behavior for the centerline density and velocity decay, once the downstream coordinate is normalized by an effective diameter, depending on the initial density ratio. Overall, these results indicate a weak influence of the density ratio and thermodynamic conditions on the similarity properties of round jets. As discussed in the paper this conclusion should be moderated by the fact that the thermodynamic conditions in the chamber are close to that of a perfect gas, so that once turbulence enhances mixing, these SC jets behave like low-pressure jets. However, in the dense-core and transition regions the influence of the thermodynamic conditions is clear: the jet with most real-gas effects has a longer dense core and a slower transition to turbulence. This highlights the necessity to implement real-gas thermodynamics for the numerical simulation of SC flows, not only to obtain accurate values for the density, but also to capture the structure of the flow.

Acknowledgments

The funding for this research is provided by Snecma, which is the prime contractor for European launcher Ariane 5 cryogenic propulsion systems, and Centre National d'Etude Spatiale and is gratefully acknowledged. This work was granted access to the high-performance computing resources of Centre Informatique National de l'Enseignement Supérieur under the allocation 2009-x2009025082 made by Grand Equipement National de Calcul Intensif.

References

[1] Meng, H., and Yang, V., "A Unified Treatment of General Fluid Thermodynamics and Its Application to a Preconditioning Scheme," *Journal of Computational Physics*, Vol. 189, No. 1, 2003, pp. 277–304. doi:10.1016/S0021-9991(03)00211-0

[2] Bellan, J., "Supercritical (and Subcritical) Fluid Behavior and Modeling: Drops, Streams, Shear and Mixing Layers, Jets and Sprays," *Progress in Energy and Combustion Science*, Vol. 26, Nos. 4–6, 2000, pp. 329–366. doi:10.1016/S0360-1285(00)00008-3

[3] Oefelein, J. C., and Yang, V., "Modeling High-Pressure Mixing and Combustion Processes in Liquid Rocket Engines," *Journal of Propulsion and Power*, Vol. 14, No. 5, 1998, pp. 843–857. doi:10.2514/2.5349

[4] Yang, V., "Modeling of Supercritical Vaporization, Mixing, and Combustion Processes in Liquid-Fueled Propulsion Systems," *Proceedings of the Combustion Institute*, Vol. 28, No. 1, 2000, pp. 925–942. doi:10.1016/S0082-0784(00)80299-4

[5] Poling, B. E., Prausnitz, J. M., and O'Connel, J. P., *The Properties of Gases and Liquids*, 5th ed., McGraw–Hill, New York, 2001.

[6] Davis, D. W., and Chehroudi, B., "Measurements in an Acoustically-Driven Coaxial Jet Under Sub-, Near-, and Supercritical Conditions," *Journal of Propulsion and Power*, Vol. 23, No. 2, 2007, pp. 364–374. doi:10.2514/1.19340

[7] Bellan, J., "Theory, Modeling and Analysis of Turbulent Supercritical Mixing," *Combustion Science and Technology*, Vol. 178, Nos. 1–3, 2006, pp. 253–281. doi:10.1080/00102200500292241

[8] Harstad, K., and Bellan, J., "High-Pressure Binary Mass Diffusion Coefficients for Combustion Applications," *Industrial and Engineering Chemistry Research*, Vol. 43, No. 2, 2004, pp. 645–654. doi:10.1021/ie0304558

[9] Oschwald, M., Smith, J. J., Branam, R., Hussong, J., Shick, A., Chehroudi, B., and Talley, D., "Injection of Fluids into Supercritical Environments," *Combustion Science and Technology*, Vol. 178, Nos. 1–3, 2006, pp. 49–100. doi:10.1080/00102200500292464

[10] Branam, R., and Mayer, W., "Characterisation of Cryogenic Injection at Supercritical pressure," *Journal of Propulsion and Power*, Vol. 19, No. 3, May–June 2003, pp. 342–355. doi:10.2514/2.6138

[11] Chehroudi, B., Talley, D., and Coy, E., "Visual Characteristics and Initial Growth Rate of Round Cryogenic Jets at Subcritical and Supercritical Pressures," *Physics of Fluids*, Vol. 14, No. 2, Feb. 2002, pp. 850–861. doi:10.1063/1.1430735

[12] Zong, N., Meng, H., Hsieh, S.-Y., and Yang, V., "A Numerical Study of Cryogenic Fluid Injection and Mixing Under Supercritical Conditions," *Physics of Fluids*, Vol. 16, No. 12, 2004, pp. 4248–4261. doi:10.1063/1.1795011

[13] Selle, L. C., Okong'o, N. A., Bellan, J., and Harstad, K. G., "Modelling of Subgrid-Scale Phenomena in Supercritical Transitional Mixing Layers: An A Priori study," *Journal of Fluid Mechanics*, Vol. 593, 2007, pp. 57–91.

[14] Oschwald, M., and Schik, A., "Supercritical Nitrogen Free Jet Investigated by Spontaneous Raman Scattering," *Experiments in Fluids*, Vol. 27, 1999, pp. 497–506. doi:10.1007/s003480050374

[15] Mayer, W., Tellar, J., Branam, R., Schneider, G., and Hussong, J., "Raman Measurements of Cryogenic Injection at Supercritical Pressure," *Heat and Mass Transfer*, Vol. 39, Nos. 8–9, 2003, pp. 709–719. doi:10.1007/s00231-002-0315-x

[16] Oschwald, M., and Micci, M. M., "Spreading Angle and Centerline Variation of Density of Supercritical Nitrogen Jets," *Atomization and Sprays*, Vol. 12, Nos. 1–3, 2002, pp. 91–106. doi:10.1615/AtomizSpr.v12.i123.50

[17] Chehroudi, B., Cohn, R., and Talley, D., "Cryogenic Shear Layers: Experiments and Phenomenological Modeling of the Initial Growth Rate Under Subcritical and Supercritical Conditions," *International Journal of Heat and Fluid Flow*, Vol. 23, No. 5, Oct. 2002, pp. 554–563. doi:10.1016/S0142-727X(02)00151-0

[18] Zong, N., "Modeling and Simulation of Cryogenic Fluid Injection and Mixing Dynamics Under Supercritical Conditions," Ph.D. Thesis, Dept. of Mechanical and Nuclear Engineering, Pennsylvania State Univ., State College, PA, 2005.

[19] Zong, N., and Yang, V., "Cryogenic Fluid Jets and Mixing Layers in Transcritical and Supercritical Environments," *Combustion Science and Technology*, Vol. 178, Nos. 1–3, 2006, pp. 193–227. doi:10.1080/00102200500287613

[20] Chen, C. J., and Rodi, W., *Vertical Turbulent Buoyant Jets: A Review of Experimental Data*, Pergamon, New York, 1980.

[21] Oefelein, J. C., "Thermophysical Characteristics of Shear-Coaxial Lox-H2 Flames at Supercritical Pressure," *Proceedings of the Combustion Institute*, Vol. 30, No. 2, 2005, pp. 2929–2937. doi:10.1016/j.proci.2004.08.212

[22] Oefelein, J. C., "Mixing and Combustion of Cryogenic Oxygen-Hydrogen Shear-Coaxial Jet Flames at Supercritical Pressure," *Combustion Science and Technology*, Vol. 178, Nos. 1–3, 2006, pp. 229–252. doi:10.1080/00102200500325322

[23] Matsuyama, S., Shinjo, J., Mizobuchi, Y., and Ogawa, S., "A Numerical Investigation on Shear Coaxial LOx/GH2 Jet Flame at Supercritical Pressure," 44th AIAA Aerospace Sciences Meeting and Exhibit, Reno, NV, AIAA Paper 761, 2006.

[24] Tramecourt, N., Menon, S., Lal, M., and Amaya, J., "Controllable Atomization for Supercritical Combustion: A Combined Experimental and Numerical Study," Georgia Inst. of Technology, Computational Combustion Lab., Rept. 2004-011, Atlanta, 2004.

[25] Chassaing, P., "Mélange Turbulent de gaz Inertes dans un Jet de Tube Libre," Ph.D. Thesis, Institut National Polytechnique de Toulouse, Toulouse, France, 1979.

[26] Pitts, W. M., "Effects of Global Density Ratio on the Centerline Mixing Behavior of Axisymmetric Turbulent Jets," *Experiments in Fluids*, Vol. 11, 1991, pp. 125–134.

[27] Richards, C. D., and Pitts, W. M., "Global Density Effects on the Self-Preservation Behavior of Turbulent Free Jets," *Journal of Fluid Mechanics*, Vol. 254, 1993, pp. 417–435. doi:10.1017/S0022112093002204

[28] Panchapakesan, N. R., and Lumley, J. L., "Turbulence Measurements in Axisymmetric Jets of Air and Helium," *Journal of Fluid Mechanics*, Vol. 246, 1993, pp. 197–247. doi:10.1017/S0022112093000096

[29] Amielh, M., Djeridane, T., Anselmet, F., and Fulachier, L., "Velocity Near-Field of Variable Density Turbulent Jets," *International Journal of Heat and Mass Transfer*, Vol. 39, No. 10, 1996, pp. 2149–2164. doi:10.1016/0017-9310(95)00294-4

[30] Hussein, H. J., Capp, S. P., and George, W. K., "Velocity Measurements in a High- Reynolds-Number, Momentum-Conservative, Axisymmetric, Turbulent Jet" *Journal of Fluid Mechanics*, Vol. 258, 1994, pp. 31–75. doi:10.1017/S002211209400323X

[31] Peng, D. Y., and Robinson, D. B., "A New Two-Constant Equation of State," *Industrial and Engineering Chemistry Fundamentals*, Vol. 15, No. 1, 1976, pp. 59–64. doi:10.1021/i160057a011

[32] Miller, R. S., Harstad, K. G., and Bellan, J., "Direct Numerical Simulation of Supercritical Fluid Mixing Layers Applied to Heptane-Nitrogen," *Journal of Fluid Mechanics*, Vol. 436, 2001, pp. 1–39.

[33] "NIST-JANAF Thermochemical Tables," National Inst. of Standards and Technology, Gaithersburg, MD, 1998.

[34] Keizer, J., *Statistical Thermodynamics of Nonequilibrium Processes*, Springer–Verlag, New York, 1987.

[35] Miller, R. S., Harstad, K., and Bellan, J., "Evaluation of Equilibrium and Nonequilibrium Evaporation Models for Many-Droplet Gas-Liquid Flow Simulations," *International Journal of Multiphase Flow*, Vol. 24, No. 6, 1998, pp. 1025–1055. doi:10.1016/S0301-9322(98)00028-7

[36] Harstad, K., and Bellan, J., "The Lewis Number Under Supercritical Conditions," *International Journal of Heat and Mass Transfer*, Vol. 42, No. 6, 1999, pp. 961–970. doi:10.1016/S0017-9310(98)00230-0

[37] Harstad, K., and Bellan, J., "An All-Pressure Fluid Drop Model Applied to a Binary Mixture: Heptane in Nitrogen," *International Journal of Multiphase Flow*, Vol. 26, No. 10, Oct. 2000, pp. 1675–1706. doi:10.1016/S0301-9322(99)00108-1

[38] Chung, T. H., Ajlan, M., Lee, L. L., and Starling, K. E., "Generalized Multiparameter Correlation for Nonpolar and Polar Fluid Transport Properties," *Industrial and Engineering Chemistry Research*, Vol. 27, No. 4, 1988, pp. 671–679. doi:10.1021/ie00076a024

[39] Nicoud, F., and Ducros, F., "Subgrid-Scale Stress Modelling Based on the Square of the Velocity Gradient Tensor," *Flow, Turbulence and Combustion*, Vol. 62, No. 3, 1999, pp. 183–200. doi:10.1023/A:1009995426001

[40] Moin, P., Squires, K. D., Cabot, W., and Lee, S., "A Dynamic Subgrid-Scale Model for Compressible Turbulence and Scalar Transport," *Physics of Fluids A*, Vol. 3, No. 11, 1991, pp. 2746–2757. doi:10.1063/1.858164

[41] Moureau, V., Lartigue, G., Sommerer, Y., Angelberger, C., Colin, O., and Poinsot, T., "High-Order Methods for DNS and LES of Compressible Multi-Component Reacting Flows on Fixed and Moving Grids," *Journal of Computational Physics*, Vol. 202, No. 2, 2005, pp. 710–736. doi:10.1016/j.jcp.2004.08.003

[42] Kravchenko, A. G., and Moin, P., "On the Effect of Numerical Errors in Large Eddy Simulations of Turbulent Flows," *Journal of Computational Physics*, Vol. 131, 1997, pp. 310–322. doi:10.1006/jcph.1996.5597

[43] Gullbrand, J., and Chow, F. K., "The Effect of Numerical Errors of Turbulence Models in Large Eddy Simulations of Channel Flow, with and Without Explicit Filtering," *Journal of Fluid Mechanics*, Vol. 495, 2003, pp. 323–341. doi:10.1017/S0022112003006268

[44] Colin, O., and Rudgyard, M., "Development of High-Order Taylor-Galerkin Schemes for Unsteady Calculations," *Journal of Computational Physics*, Vol. 162, No. 2, 2000, pp. 338–371. doi:10.1006/jcph.2000.6538

[45] Selle, L., Lartigue, G., Poinsot, T., Koch, R., Schildmacher, K.-U., Krebs, W., Prade, B., et al. "Compressible Large-Eddy Simulation of Turbulent Combustion in Complex Geometry on Unstructured Meshes," *Combustion and Flame*, Vol. 137, No. 4, 2004, pp. 489–505. doi:10.1016/j.combustflame.2004.03.008

[46] Jameson, A., Schmidt, W., and Turkel, E., "Numerical Solution of the Euler Equations by Finite Volume Methods Using Runge-Kutta Time Stepping Schemes," 14th Fluid and Plasma Dynamic Conference, AIAA Paper 81-1259, 1981.

[47] Poinsot, T., and Lele, S., "Boundary Conditions for Direct Simulations of Compressible Viscous Flows," *Journal of Computational Physics*, Vol. 101, No. 1, 1992, pp. 104–129. doi:10.1016/0021-9991(92)90046-2

[48] Okong'o, N., and Bellan, J., "Consistent Boundary Conditions for Multicomponent Real Gas Mixtures Based on Characteristic Waves," *Journal of Computational Physics*, Vol. 176, No. 2, 2002, pp. 330–344. doi:10.1006/jcph.2002.6990

[49] Hirschfelder, J., Curtiss, C., and Bird, B., *Molecular Theory of Gases and Liquids*, Wiley, New York, 1954.

[50] Kraichnan, R., "Diffusion by a Random Velocity Field," *Physics of Fluids*, Vol. 13, 1970, pp. 22–31. doi:10.1063/1.1692799

[51] Smirnov, A., Shi, S., and Celik, I., "Random Flow Generation Technique for Large Eddy Simulations and Particle-Dynamics Modeling," *Journal of Fluids Engineering*, Vol. 123, 2001, pp. 359–371. doi:10.1115/1.1369598

[52] Thring, M. W., and Newby, M. P., "Combustion Length of Enclosed Turbulent Jet Flames," *Fourth Symposium (International) on Combustion*, Combustion Inst., Pittsburgh, PA, 1953, pp. 789–796.

C. Bailly
Associate Editor